

# Functionalized Iron–Nitrogen–Carbon Electrocatalyst Provides a Reversible Electron Transfer Platform for Efficient Uranium Extraction from Seawater

Hui Yang, Xiaolu Liu, Mengjie Hao, Yinghui Xie, Xiangke Wang,\* He Tian,\*  
Geoffrey I. N. Waterhouse, Paul E. Kruger, Shane G. Telfer, and Shengqian Ma\*

Uranium extraction from seawater provides an opportunity for sustainable fuel supply to nuclear power plants. Herein, an adsorption–electrocatalysis strategy is demonstrated for efficient uranium extraction from seawater using a functionalized iron–nitrogen–carbon (Fe–N<sub>x</sub>–C–R) catalyst, comprising N-doped carbon capsules supporting FeN<sub>x</sub> single-atom sites and surface chelating amidoxime groups (R). The amidoxime groups bring hydrophilicity to the adsorbent and offer surface-specific binding sites for UO<sub>2</sub><sup>2+</sup> capture. The site-isolated FeN<sub>x</sub> centres reduce adsorbed UO<sub>2</sub><sup>2+</sup> to UO<sub>2</sub><sup>+</sup>. Subsequently, through electrochemical reduction of the FeN<sub>x</sub> sites, unstable U(V) ions are reoxidized to U(VI) in the presence of Na<sup>+</sup> resulting in the generation of solid Na<sub>2</sub>O(UO<sub>3</sub>·H<sub>2</sub>O)<sub>x</sub>, which can easily be collected. Fe–N<sub>x</sub>–C–R reduced the uranium concentration in seawater from ≈3.5 ppb to below 0.5 ppb with a calculated capacity of ≈1.2 mg g<sup>-1</sup> within 24 h. To the best of the knowledge, the developed system is the first to use the adsorption of uranyl ions and electrodeposition of solid Na<sub>2</sub>O(UO<sub>3</sub>·H<sub>2</sub>O)<sub>x</sub> for the extraction of uranium from seawater. The important discoveries guide technology development for the efficient extraction of uranium from seawater.

interim technology in the transition away from fossil fuel energy.<sup>[2]</sup> Nuclear reactors are fueled by <sup>235</sup>U, which is typically concentrated from mined uranium ore. However, estimates suggest that globally there are only ≈4.5 million tons of uranium ore on land, which represents a significant obstacle to the increased implementation of nuclear power.<sup>[3]</sup> However, uranium (present as uranyl ions) is abundant in seawater, and estimates suggest ≈4.5 billion tons are available in the oceans. This makes the extraction of uranium from seawater a priority if humans want to harness nuclear energy in the future.<sup>[4]</sup>

Recently, much research effort has been focused on developing high capacity adsorbents that can recover uranium from seawater at good rates.<sup>[5]</sup> Porous materials such as metal oxides/sulfides,<sup>[6]</sup> porous organic polymers,<sup>[7]</sup> porous aromatic frameworks,<sup>[8]</sup> metal–organic frameworks,<sup>[9]</sup> biomass-based materials,<sup>[10]</sup> cova-

lent organic frameworks,<sup>[11]</sup> and porous carbons<sup>[12]</sup> have all been explored as potential adsorbents for extracting uranium from seawater. It was found that the adsorption capacity and uranyl ion-binding affinity of sorbents can be significantly improved

## 1. Introduction

Sustainable technologies are needed to meet our future energy needs.<sup>[1]</sup> Nuclear power has long been considered a practical

H. Yang, X. L. Liu, M. J. Hao, Y. H. Xie, X. K. Wang  
College of Environmental Science and Engineering  
North China Electric Power University  
Beijing 102206, P. R. China  
E-mail: xkwang@ncepu.edu.cn


H. Tian  
State Key Laboratory of Silicon Materials  
Center of Electron Microscopy  
School of Materials Science and Engineering  
Zhejiang University  
Hangzhou 310027, P. R. China  
E-mail: hetian@zju.edu.cn

G. I. N. Waterhouse  
MacDiarmid Institute for Advanced Materials and Nanotechnology  
School of Chemical Sciences  
The University of Auckland  
Auckland 1142, New Zealand

P. E. Kruger  
MacDiarmid Institute for Advanced Materials and Nanotechnology  
School of Physical and Chemical Sciences  
University of Canterbury  
Christchurch 8140, New Zealand

S. G. Telfer  
MacDiarmid Institute for Advanced Materials and Nanotechnology  
Institute of Fundamental Sciences  
Massey University  
Palmerston North 4442, New Zealand

S. Ma  
Department of Chemistry  
University of North Texas  
Denton, TX 76201, USA  
E-mail: shengqian.ma@unt.edu

 The ORCID identification number(s) for the author(s) of this article can be found under <https://doi.org/10.1002/adma.202106621>.

DOI: 10.1002/adma.202106621

by introducing specific surface functional groups onto the adsorbent such as amines,<sup>[9d]</sup> hydroxyl groups,<sup>[12c,13]</sup> carboxylic acids,<sup>[12a,14]</sup> and particularly amidoximes.<sup>[7d,e,15]</sup> Efficient uranium extraction also benefits from porous sorbents with particular pore geometries and entrained functional groups, thus promoting strong adsorbate–adsorbent interactions and facilitating mass transport. However, the adsorption of uranium ions in the pores and channels of the adsorbents can lead to pore blocking, which lowers the uranium adsorption capacity and hinders uranium recovery and adsorbent reuse. In a notable recent contribution, an electrochemical method was reported for the efficient extraction of uranium from spiked seawater.<sup>[16]</sup> The hexavalent uranyl ion ( $\text{UO}_2^{2+}$ ) was reduced to the insoluble tetravalent compound  $\text{UO}_2$  on the electrode surface at a voltage of  $-5$  to  $0$  V. While this work revealed a promising new strategy for uranium extraction, significant improvements in uranium adsorption should be possible through increasing both the adsorption capacity and electrocatalytic reduction/oxidation performance of the electrode materials used.

Porphyrin-like metal–nitrogen–carbon (M–N–C) nanomaterials have emerged as high-performance electrocatalysts in many applications, with Fe–N–C demonstrating outstanding performance for the oxygen reduction reaction (ORR).<sup>[17]</sup> The high catalytic activity of Fe–N–C for ORR can be attributed to the reversible electron transfer of the atomically dispersed  $\text{FeN}_x$  sites and redox cycling between  $\text{Fe}^{3+}$  and  $\text{Fe}^{2+}$  oxidation states. By designing and synthesizing a new material that synergistically combines uranyl adsorption with electrocatalytic activity, we developed herein a very efficient adsorption–electrocatalysis system for uranium extraction from seawater. In brief, hollow nitrogen-doped carbon capsules supporting iron single-atom sites (Fe–N<sub>x</sub>–C) were first synthesized, then functionalized with amidoxime groups (collectively denoted as R). The amidoxime groups impart hydrophilicity and a high binding affinity for  $\text{UO}_2^{2+}$ , while the site-isolated iron centers ( $\text{FeN}_x$  species) reduce the U(VI) in  $\text{UO}_2^{2+}$  to U(V) in  $\text{UO}_2^+$ . Subsequently, we discovered that the unstable U(V) of the pentavalent  $\text{UO}_2^+$  ions could be reoxidized to U(VI) in the presence of  $\text{Na}^+$ , which led to the formation of  $\text{Na}_2\text{O}(\text{UO}_3 \cdot \text{H}_2\text{O})_x$  precipitates. The latter formed as a loosely attached thick yellow deposit on the Fe–N<sub>x</sub>–C–R electrode, thus allowing easy recovery. Intuitively, reversible single electron transfer between a  $\text{FeN}_x$  site and  $\text{UO}_2^{x+}$ , as well as the presence of sodium ions, resulted in the selective formation of  $\text{Na}_2\text{O}(\text{UO}_3 \cdot \text{H}_2\text{O})_x$  during the electrocatalysis process. Based on these important discoveries, a uranium uptake capacity of  $128 \text{ mg g}^{-1}$  was achieved in 10 ppm uranyl-spiked seawater was realized using the electrocatalytic process. Fe–N<sub>x</sub>–C–R was able to reduce the uranium concentration in natural seawater (initial uranium concentration  $\approx 3.5$  ppb) to less than 0.5 ppb within 24 h (extraction capacity of  $\approx 1.2 \text{ mg g}^{-1}$ ). Further, the adsorbent–electrocatalyst exhibited excellent durability and reusability.

## 2. Results and Discussion

The ability of Fe–N<sub>x</sub>–C–R (Figure 1) to adsorb uranyl ions and further electrochemically deposit uranium in the form of insoluble precipitates was crucial in the current study for uranium

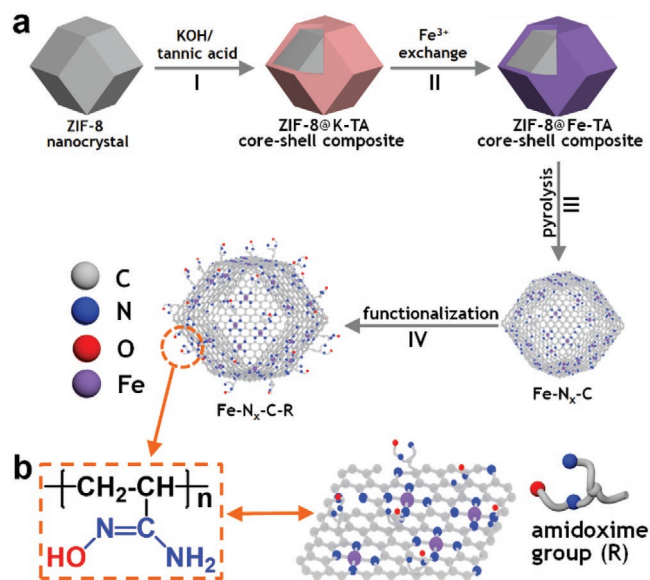


**Figure 1.** a) Schematic illustration of the synthesis of Fe–N<sub>x</sub>–C–R. b) A schematic showing the polypropylene amidoxime attached to the surface of Fe–N<sub>x</sub>–C. Hydrogen atoms have been omitted for clarity in the cartoons.

removal from seawater. To address this challenge, the surfaces of the hollow iron–nitrogen–carbon capsules (Fe–N<sub>x</sub>–C) were functionalized with amidoxime groups (denoted as R) through coating a thin layer of polypropylene amidoxime. Figure 1 describes the stepwise fabrication of Fe–N<sub>x</sub>–C–R. ZIF-8 nanocrystals were first synthesized, then coated with a potassium–tannic acid coordination polymer (Figure 1a, step I).<sup>[17d,18]</sup> The potassium ions in the tannic acid polymer were then exchanged for  $\text{Fe}^{3+}$  ions to give ZIF-8@Fe-TA (Figure 1a, step II, Figures S1–S5, Supporting Information). Fourier transform infrared (FTIR) spectroscopy verified the formation of metal/tannic shells on ZIF-8 nanocrystals (Figure S8, Supporting Information). The composite was further heated at  $950^\circ\text{C}$  in an argon atmosphere, yielding Fe–N<sub>x</sub>–C. Scanning electron microscopy (SEM) and transmission electron microscopy (TEM) were employed to observe the morphology of Fe–N<sub>x</sub>–C, which comprised hollow dodecahedral capsules with a wall thickness of about 10 nm (Figure 2a; Figure S6, Supporting Information). Low magnification HAADF–STEM and corresponding energy dispersive X-ray spectroscopy (EDS) images show that Fe, C, and N were homogeneously distributed over the capsules (Figure 2b–f). No detectable zinc was found in Fe–N<sub>x</sub>–C. During the high-temperature pyrolysis step, the zinc(II) ions of ZIF-8 were reduced to metallic Zn, which subsequently vaporized and escaped from the capsules. Aberration–corrected HAADF–STEM further revealed the presence of highly dispersed bright dots, confirming the presence of atomically dispersed iron species on the N-doped carbon support. (Figure 2g). No large aggregates or nanoparticles were detected in the images.

Subsequently, amidoxime functional groups were attached to the carbon capsules. To achieve this, Fe–N<sub>x</sub>–C was treated in a freshly prepared polyacrylonitrile/azobisisobutyronitrile/N, N–dimethylformamide (DMF) solution to create a precursor-loaded

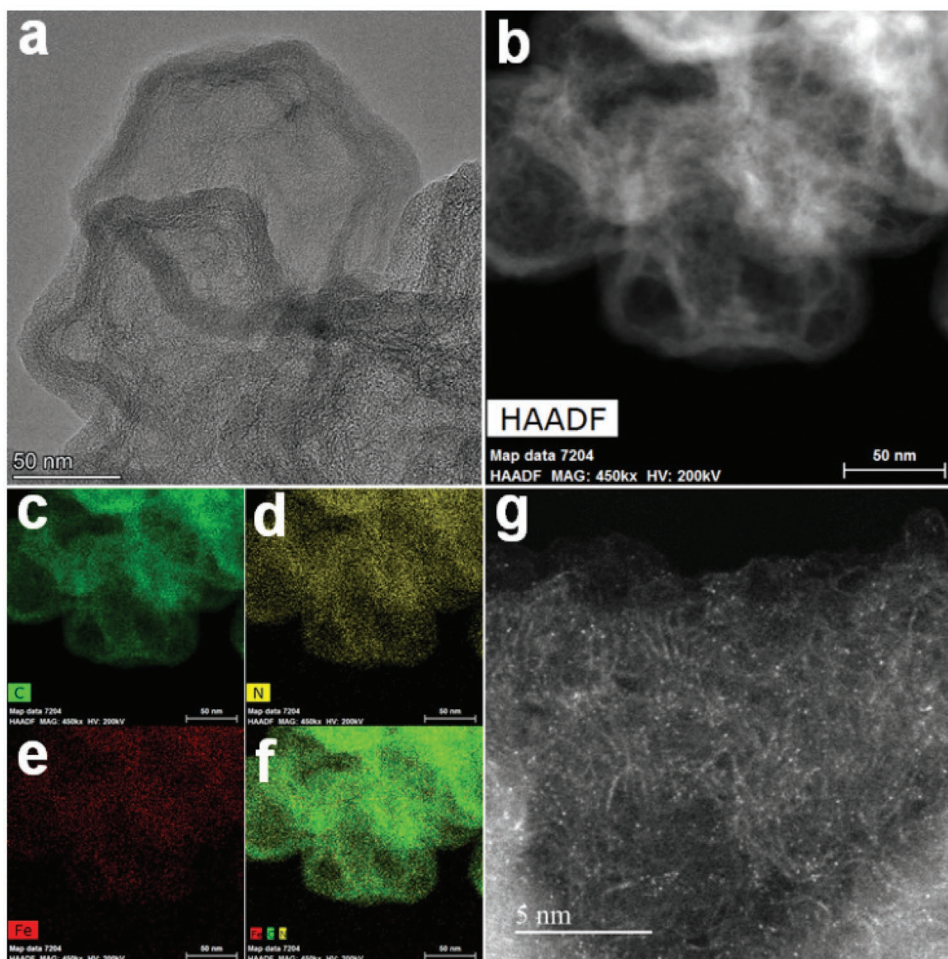


**Figure 2.** a,b) TEM and HAADF-STEM images of Fe-N<sub>x</sub>-C. c-f) Corresponding EDS maps reveal a homogeneous distribution of C (green), N (yellow), and Fe (red) over the carbon capsules. g) Aberration-corrected HAADF-STEM image of Fe-N<sub>x</sub>-C, showing the atomically dispersed iron. The scale bars in (b)–(f) represent 50 nm.

composite with -CN groups attached on the surface of the hollow iron-nitrogen-carbon capsules. Subsequent treatment with hydroxylamine in H<sub>2</sub>O produced a thin layer of polypropylene amidoxime coated Fe-N<sub>x</sub>-C (denoted as Fe-N<sub>x</sub>-C-R), with amidoxime groups on the surface of the hollow iron-nitrogen-carbon capsules. (Figure 1a,b, step IV, Scheme S1, Supporting Information). The FTIR spectrum of Fe-N<sub>x</sub>-C-R showed the appearance of a nitrile stretch (2246 cm<sup>-1</sup>) after the polyacrylonitrile/azobisisobutyronitrile/DMF treatment. This peak disappeared after reaction with hydroxylamine, whilst new peaks appeared due to C=N (1650 cm<sup>-1</sup>), C-N (1390 cm<sup>-1</sup>), and N-O (930 cm<sup>-1</sup>). These new peaks confirmed the successful introduction of amidoxime groups (Figure 3a).<sup>[7e,11e]</sup> TEM and SEM images showed that Fe-N<sub>x</sub>-C-R retained the characteristic hollow dodecahedral morphology of Fe-N<sub>x</sub>-C (Figure 3b; Figure S7, Supporting Information). Spherical aberration-corrected HAADF-STEM imaging showed a high density of isolated bright spots, confirming that atomically dispersed iron sites were still firmly anchored on the hollow carbon capsules (Figure 3c). HAADF-STEM and mapping images for C, N, O, and Fe showed all of the elements were uniformly dispersed in Fe-N<sub>x</sub>-C-R (Figure 3d–i).

The structures of Fe-N<sub>x</sub>-C-R and Fe-N<sub>x</sub>-C were further investigated by powder X-ray diffraction (PXRD), X-ray photoelectron spectroscopy (XPS), Raman spectroscopy, X-ray absorption spectroscopy (XAS), and iron (<sup>57</sup>Fe) Mössbauer spectroscopy. The PXRD patterns for each sample display broad peaks around 24° and 44°, corresponding to the graphitic carbon domains in these materials (Figure S2, Supporting Information). The C 1s XPS spectrum of Fe-N<sub>x</sub>-C contained peaks due to semigraphitic carbon C=C/C-C bonds (284.6 eV), C-N bonds (285.7 eV), C=O bonds (287.5 eV), and π-π\* transitions (290 eV) (Figure 4a). Four types of N environments were found in Fe-N<sub>x</sub>-C, including pyridinic-N (398.3 eV), pyrrolic-N (400.1 eV), graphitic-N (401.1 eV), and N-O moieties (404.6 eV) (Figure 4b). The C 1s spectrum of Fe-N<sub>x</sub>-C-R (Figure 4c) was similar to that of Fe-N<sub>x</sub>-C, except for the increase of the peak at 285.9 eV due to the amidoxime groups.<sup>[19]</sup> Comparing the N 1s signals of Fe-N<sub>x</sub>-C and Fe-N<sub>x</sub>-C-R, the latter contained less graphitic-N and pyridinic-N (Figure 4d). However, the amount of pyrrolic-N and oxidized-N (N-O<sub>x</sub>) in Fe-N<sub>x</sub>-C-R was significantly increased (Figure 4d). The O 1s spectrum of Fe-N<sub>x</sub>-C-R was deconvoluted into two subpeaks, which are assigned to C=O (531.3 eV) and N-O-H (532.2 eV) species

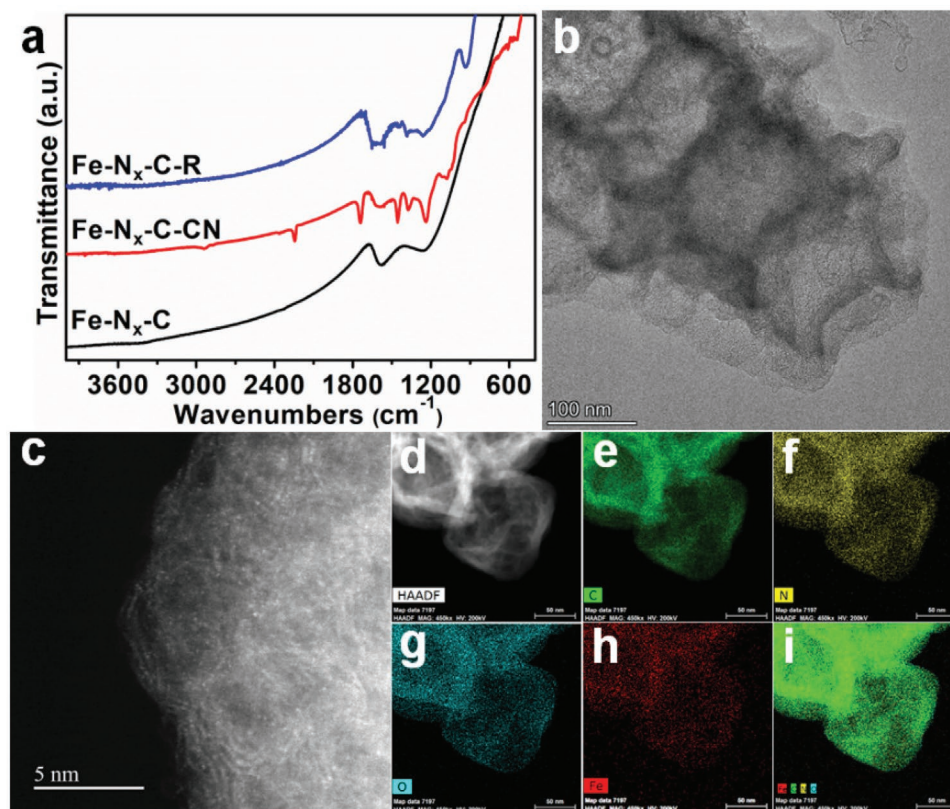


**Figure 3.** a) FTIR spectra of different materials. b,c) TEM and aberration-corrected HAADF-STEM images of Fe-N<sub>x</sub>-C-R. d-i) HAADF-STEM image of Fe-N<sub>x</sub>-C-R and corresponding EDS maps revealing the homogeneous distribution of C (green), N (yellow), O (cyan), and Fe (red) throughout the sample. The scale bars in (d)–(i) represent 50 nm.

(Figure 4e).<sup>[15a,20]</sup> The normalized X-ray absorption near edge structure (XANES) spectra for Fe-N<sub>x</sub>-C and Fe-N<sub>x</sub>-C-R were similar to that of Fe-tetraphenylporphyrin (FeTPP), showing a distinctive pre-edge feature at 7115.1 eV. This suggests that the iron atoms in Fe-N<sub>x</sub>-C and Fe-N<sub>x</sub>-C-R are stabilized in a strict square-planar configuration (i.e., FeN<sub>4</sub>) with *D*<sub>4h</sub> symmetry (Figure 4f). The Fourier-transformed extended X-ray absorption fine structure (FT-EXAFS) spectra of the samples showed a sharp peak around 1.5 Å in *R* space, which again parallels the FeTPP reference (Figure 4g). The EXAFS fitting results of Fe-N<sub>x</sub>-C-R confirmed the FeN<sub>4</sub> coordination, with each iron center being connected by four N atoms with a Fe-N length of 2.05(8) Å (Figure 4h; Table S1, Supporting Information). Subsequently, <sup>57</sup>Fe Mössbauer spectroscopy measurements were conducted on Fe-N<sub>x</sub>-C-R to gain a deeper understanding of the electronic state of Fe in the material. The spectrum was fitted with the D1 and D2 double peaks, which can be assigned to the porphyrin-like Fe<sup>2+</sup>-N<sub>4</sub> coordination sites, where Fe<sup>2+</sup> is in low and medium-spin states, respectively (Figure 4i).<sup>[21]</sup> Raman spectroscopy established that Fe-N<sub>x</sub>-C-R contained both graphitic sp<sup>2</sup> carbon at 1590 cm<sup>-1</sup> and disordered sp<sup>3</sup> carbon at 1350 cm<sup>-1</sup> (Figure S9, Supporting Information). Taken together, this suite of experiments confirms that the surface of Fe-N<sub>x</sub>-C-R is rich in amidoxime-containing functional groups and porphyrin-like FeN<sub>4</sub> single-atom sites.

The permanent porosity of Fe-N<sub>x</sub>-C-R was probed by N<sub>2</sub> adsorption experiments at 77 K. The isotherms showed typical

type IV behavior (Figure S10, Supporting Information), suggesting the coexistence of hierarchical pore structures. Pronounced hysteresis loops were observed, indicating the existence of ink bottle shape mesopores. The measured BET surface area of Fe-N<sub>x</sub>-C-R (366 m<sup>2</sup> g<sup>-1</sup>) was much less than Fe-N<sub>x</sub>-C (836 m<sup>2</sup> g<sup>-1</sup>). The corresponding pore size distribution analysis results demonstrated that Fe-N<sub>x</sub>-C-R contained both micropores and mesopores with diameters clustered around 1.8 and 2.3 nm, respectively (Figures S11 and S12, Supporting Information). Fe-N<sub>x</sub>-C-R and Fe-N<sub>x</sub>-C contained 1.18 and 1.32 wt.% of iron, respectively, as determined by inductively coupled plasma mass spectrometry (ICP-MS) tests. The surface wettability properties of Fe-N<sub>x</sub>-C-R and Fe-N<sub>x</sub>-C were characterized by contact angle measurements. The contact angle of water droplets on Fe-N<sub>x</sub>-C was 126°, whereas for Fe-N<sub>x</sub>-C-R the water contact angle was much lower at around 40° (Figure 5a). These results show that the surface amidoxime groups of Fe-N<sub>x</sub>-C-R significantly enhance the hydrophilicity of the material. The amidoxime groups on Fe-N<sub>x</sub>-C-R are expected to offer an abundance of accessible binding sites for the adsorption of UO<sub>2</sub><sup>2+</sup> cations. In combination with the isolated FeN<sub>x</sub> sites on the N-doped carbon capsules, Fe-N<sub>x</sub>-C-R possessed all the essential components to be an efficient adsorbent-electrocatalyst for uranium removal from seawater, which was validated by experiments below.

To evaluate the uranium extraction ability of Fe-N<sub>x</sub>-C-R, preliminary studies were conducted in spiked-seawater/uranyl

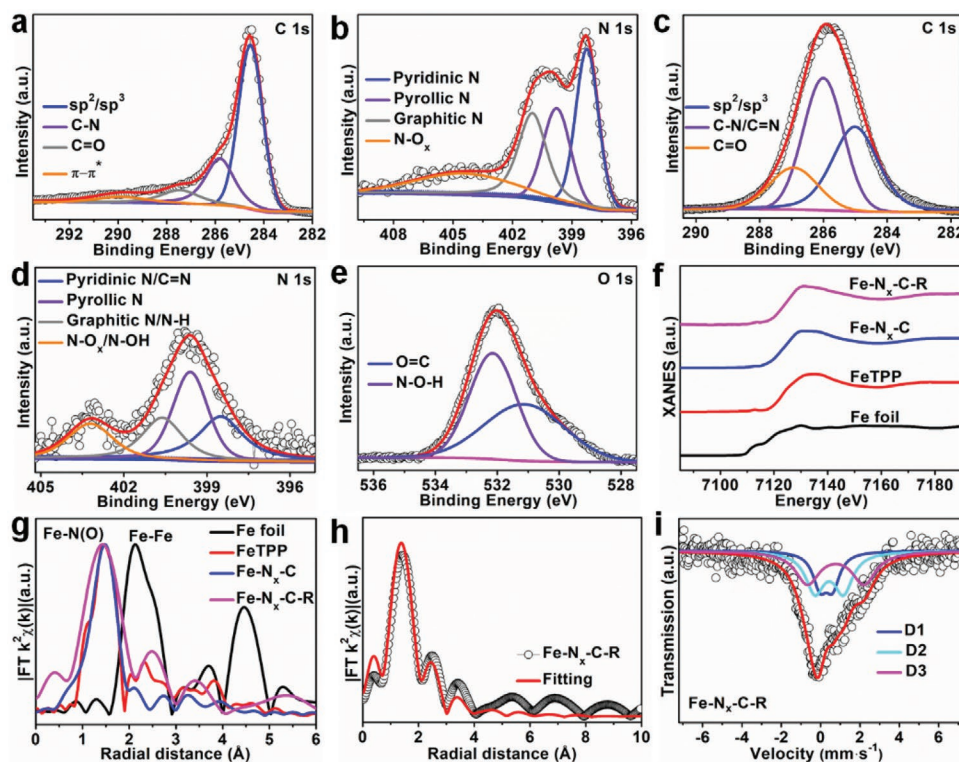


**Figure 4.** a, b) C 1s and N 1s XPS spectra for Fe-N<sub>x</sub>-C. c–e) C 1s, N 1s, and O 1s XPS spectra for Fe-N<sub>x</sub>-C–R. f) Fe K-edge XANES spectra for Fe-N<sub>x</sub>-C, Fe-N<sub>x</sub>-C–R, FeTPP, and Fe foil. g) Fourier transform (FT) EXAFS spectra for Fe-N<sub>x</sub>-C, Fe-N<sub>x</sub>-C–R, FeTPP, and Fe foil. h) Corresponding EXAFS R-space fitting curves for Fe-N<sub>x</sub>-C–R. i) <sup>57</sup>Fe Mössbauer transmission spectrum for Fe-N<sub>x</sub>-C–R. The data for Fe foil and FeTPP stands in 4f, and 4g were reported in our previous work.<sup>[17d]</sup>

ion solutions. Fe-N<sub>x</sub>-C was used for comparison purposes. Equilibrium adsorption capacities were determined in uranyl-spiked seawater solutions of different concentrations (from 0 to 20 ppm based on uranium, pH 8.1) at a fixed material-to-solution ratio of 0.1 mg mL<sup>-1</sup>. The equilibrium adsorption experiments were conducted over 24 h at 25 °C under constant shaking. The adsorption capacity of Fe-N<sub>x</sub>-C–R was tested and analyzed to be 129.9 mg g<sup>-1</sup> (Figure 5b; Table S2, Supporting Information). The equilibrium adsorption data were well-described by a Langmuir model, yielding a correlation coefficient equal to 0.97.<sup>[22]</sup> The distribution coefficient (*K<sub>d</sub>*) value was calculated to equal 3.6 × 10<sup>4</sup> mL g<sup>-1</sup>, indicating an excellent affinity toward uranyl ions. Subsequently, kinetic adsorption isotherms were determined in 10 ppm spiked-seawater uranyl solutions (pH 8.1) over periods ranging from 0 to 20 h. The result showed that Fe-N<sub>x</sub>-C–R possessed an extremely rapid uranium capture capability with a sharp upward trend (especially before 200 min), reaching greater than 70% of its equilibrium adsorption capacity after only 150 min (Figure 5c; Table S3, Supporting Information). The adsorption data were well-fitted by the pseudo-second-order kinetic model, indicating that the adsorption of uranium by Fe-N<sub>x</sub>-C–R mainly depends on chemical adsorption.<sup>[23]</sup> Overall, Fe-N<sub>x</sub>-C–R demonstrated better adsorption performance for uranyl ions than Fe-N<sub>x</sub>-C, suggesting that the amidoxime groups coordinate with the uranyl ions. XANES spectra showed that the near-edge feature of Fe-N<sub>x</sub>-C–R after uranium adsorption is allied to that of uranyl nitrate hexahydrate, suggesting that the uranium exists

in the form of U(VI)O<sub>2</sub><sup>2+</sup> (Figure 5d). EXAFS spectra and fitting results confirmed the U(VI) coordination environment is similar to a previous reported uranyl-amidoxime η<sup>2</sup>-binding motif mode, with each U center being coordinated by two axial oxygen atoms, two atoms from coordinated H<sub>2</sub>O molecules, and two oxygen atoms and nitrogen atoms from two amidoxime groups (Figure 5e; Figures S13 and S14 and Table S1, Supporting Information). Further, U 4f and O 1s XPS spectra indicated the presence of U(VI) and U = O environments after the adsorption experiment, also consistent with the presence of adsorbed uranyl ions (Figure S15, Supporting Information).<sup>[6e,15a]</sup> In comparison, the isotherms displayed a slightly faster adsorption rate and higher adsorption capacity in aqueous uranyl solutions relative to spiked seawater solutions (Figure S16, Tables S4 and S5, Supporting Information). We attributed the decrease in the uranyl adsorption rate and capacity in the spiked seawater experiments to the high ionic strength and the competitive adsorption of other ions.

Encouraged by the unique structural characteristics and uranyl ion adsorption performance, we then evaluated Fe-N<sub>x</sub>-C–R as an electrocatalyst for uranium extraction from uranyl-spiked seawater (≈10 ppm, pH 8.1) and natural seawater. We first operated cyclic voltammetry (CV) tests in natural seawater and uranyl-spiked seawater using a traditional three-electrode electrochemical cell. Figure 5f showed a sharp peak at -0.77 V (vs SCE) corresponding to the reduction of U(VI) to U(V), and a peak at -0.43 V (vs SCE) due to the oxidation of U(V) to U(VI).<sup>[24]</sup> On the basis of these results, we then studied

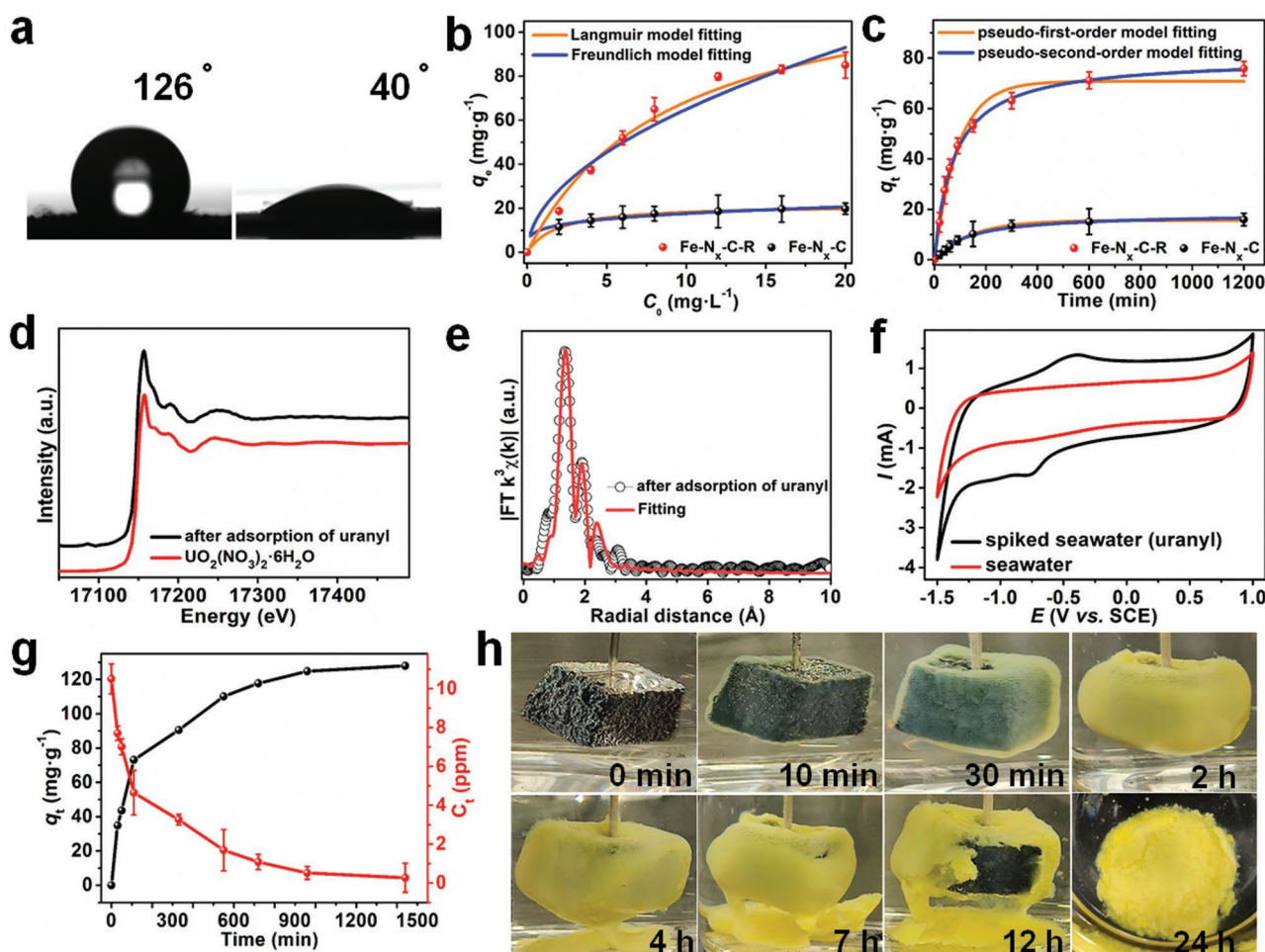


**Figure 5.** a) Contact angles for deionized water on pressed pellets of  $\text{Fe-N}_x\text{-C}$  (left) and  $\text{Fe-N}_x\text{-C-R}$  (right). b) Equilibrium adsorption isotherms for uranyl ion adsorption on different materials at a fixed material-to-solution ratio of  $0.1 \text{ mg mL}^{-1}$  in uranyl-spiked seawater (from 0 to 20 ppm). c) Uranyl ion adsorption kinetics on different materials at an initial  $\text{UO}_2^{2+}$  concentration of 10 ppm in uranyl-spiked seawater. d)  $\text{U L}_{III}$ -edge XANES spectra for  $\text{Fe-N}_x\text{-C-R}$  after adsorption of uranyl, and  $\text{UO}_2(\text{NO}_3)_2 \cdot 6\text{H}_2\text{O}$ . e)  $\text{U L}_{III}$ -edge EXAFS R-space and corresponding fitting curves for  $\text{Fe-N}_x\text{-C-R}$  after adsorption of uranyl. f) Cyclic voltammograms for uranyl-spiked seawater and natural seawater. g) Uranium extraction from spiked seawater with initial uranium concentrations of  $\approx 10 \text{ ppm}$ , using  $\text{Fe-N}_x\text{-C-R}$  as an adsorbent-electrocatalyst. h) Photographs of the  $\text{Fe-N}_x\text{-C-R}$  electrode in spiked seawater (initial uranium concentration of  $\approx 1000 \text{ ppm}$ ) during electrocatalytic extraction.

the uranium extraction performance of  $\text{Fe-N}_x\text{-C-R}$  using the square wave conversion method (Figure S17, Supporting Information). Here, a graphite rod served as the positive electrode, and  $\text{Fe-N}_x\text{-C-R}$  served as the negative electrode. Experiments were conducted by alternating the voltage between  $-5$  and  $0 \text{ V}$  at a frequency of  $400 \text{ Hz}$  during the tests.  $\text{Fe-N}_x\text{-C-R}$  removed 71%, 91%, and 99% of the uranium within 5.5, 12, and 24 h, respectively, from a 10 ppm uranyl-spiked seawater sample (Figure 5g). The experimental maximum removal capacity reached  $128 \text{ mg g}^{-1}$ , indicating a high uranium extraction efficiency. The longevity and durability of  $\text{Fe-N}_x\text{-C-R}$  were established by ten cycles of uranyl ion removal, washing and  $\text{Fe-N}_x\text{-C-R}$  reuse, with negligible loss in performance observed over the ten cycles (Figure S18, Supporting Information). The SEM image of  $\text{Fe-N}_x\text{-C-R}$  after the ten cycles exhibited that the dodecahedral morphology of the sample was retained (Figure S19, Supporting Information), implying chemical and structural robustness. FTIR spectroscopy confirmed the

amidoxime functional groups in  $\text{Fe-N}_x\text{-C-R}$  were retained after the ten cycles (Figure S20, Supporting Information). In light of the above excellent adsorption-electroextraction performances of  $\text{Fe-N}_x\text{-C-R}$ , we further carried out a uranium extraction performance test in natural seawater (the natural concentration of uranium in the sample is  $\approx 3.5 \text{ ppb}$ ). After 24 h of extraction, the detected uranium in seawater was less than  $0.5 \text{ ppb}$  (calculated capacity of  $\approx 1.2 \text{ mg g}^{-1}$  in 24 h), comparable to other high-performance sorbents (Table S6, Supporting Information), suggesting effective uranium absorption performance and obvious potential to use the adsorption-electrocatalysis system for uranium extraction in practical applications.

After demonstrating the ability of  $\text{Fe-N}_x\text{-C-R}$  to efficiently extract uranium from seawater, we investigated the extraction mechanism. A further extraction experiment was conducted in a freshly prepared 1000 ppm of uranyl-spiked seawater. As shown in Figure S21 (Supporting Information),  $\text{Fe-N}_x\text{-C-R}$  exhibited an exceptional ability to extract uranium rapidly,

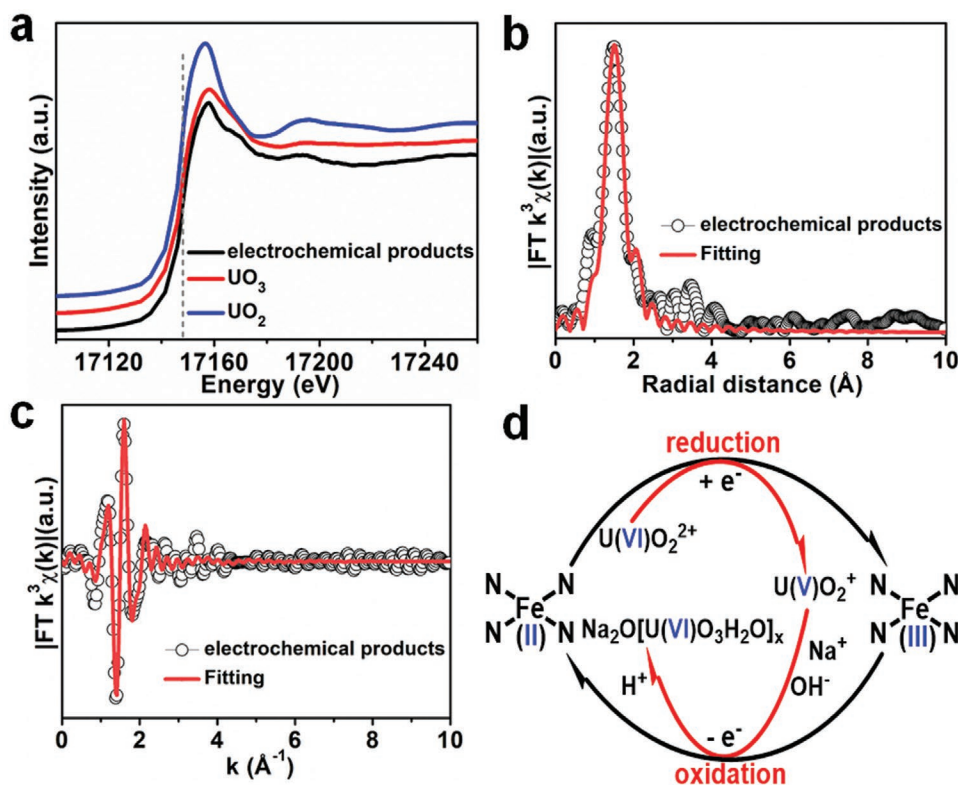


**Figure 6.** a) U L<sub>III</sub>-edge XANES spectra for electrochemically produced products using Fe–N<sub>x</sub>–C–R as the catalyst, together with UO<sub>3</sub> and UO<sub>2</sub> as points of comparison. b,c) FT–EXAFS spectra and corresponding R-space and k-space fitting curves for electrochemically produced products. d) Schematic showing a plausible reaction mechanism for the Fe–N<sub>x</sub>–C–R catalyzed extraction of uranium from seawater.

with the capacity determined to be 14 302 mg g<sup>-1</sup> within 24 h, suggesting that electrocatalysis effectively promoted uranyl ion conversion. A pale-yellow floc formed around the surface of the Fe–N<sub>x</sub>–C–R/carbon felt electrode within 10 min (Figure 5h). After 30 min, a darker yellow product covered the whole working electrode. As the extraction time increased up to 24 h, uranyl ions continued to be efficiently transformed into the electrodeposited precipitate, which could easily be collected from the electrode. PXRD and XPS analyses demonstrated that the yellow precipitate comprised Na<sub>2</sub>O(UO<sub>3</sub>·H<sub>2</sub>O)<sub>x</sub> (Figures S22–S24, Supporting Information). As shown in Figure 6a, XANES spectra for Na<sub>2</sub>O(UO<sub>3</sub>·H<sub>2</sub>O)<sub>x</sub> at the U L<sub>III</sub>-edge were similar to that of UO<sub>3</sub>, indicating the presence of a U(VI) dominant oxidation state (Figure 6a). The fitting of EXAFS results in R- and k-space revealed the coordination number of the U(VI) units in Na<sub>2</sub>O(UO<sub>3</sub>·H<sub>2</sub>O)<sub>x</sub> to be 6. (Figure 6b,c; Table S1, Supporting Information). No U(IV) solid products (such as UO<sub>2</sub> and/or (UO<sub>2</sub>)<sub>2</sub>) were detected, indicating that unstable U(V) was not reduced to a lower state U(IV) during the process. We noticed that the pH value of the spiked seawater solution decreased from 5.01 to 3.51, implying H<sup>+</sup> evolution during the formation of Na<sub>2</sub>O(UO<sub>3</sub>·H<sub>2</sub>O)<sub>x</sub> (n.b., the initial seawater sample had a pH of 8.1). The control experiment was further performed with deionized water in the absence of sodium ions. As expected, no Na<sub>2</sub>O(UO<sub>3</sub>·H<sub>2</sub>O)<sub>x</sub> nor any other solid precipitates were produced (Figure S25, Supporting Information). Intuitively, both sodium ions and uranyl ions are needed for the generation of

the Na<sub>2</sub>O(UO<sub>3</sub>·H<sub>2</sub>O)<sub>x</sub> precipitate under the conditions of our seawater experiments.

Based on these findings, a probable mechanism for uranium extraction from seawater by the adsorption–electrocatalysis system was developed (Figure 6d). The amidoxime functional groups on Fe–N<sub>x</sub>–C–R boosted surface hydrophilicity and enhanced uranyl ion uptake by offering an abundance of cation chelating sites. The FeN<sub>x</sub> active sites in the hollow carbon capsules (initially containing Fe(II)N<sub>4</sub>) then reduced the U(VI)O<sub>2</sub><sup>2+</sup> to U(V)O<sub>2</sub><sup>+</sup> by transferring a single electron to U(VI) during the reduction process.<sup>[24a,25]</sup> Subsequently, Na<sub>2</sub>O(UO<sub>3</sub>·H<sub>2</sub>O)<sub>x</sub> is generated by oxidation of U(V) back to U(VI) in the presence of Na<sup>+</sup>, with the concomitant liberation of protons. Meanwhile, the unstable pentavalent uranium (U(V)) transferred an electron back to the Fe(III)N<sub>4</sub> center, thereby regenerating Fe(II)N<sub>4</sub>. Overall, reversible single electron transfer between FeN<sub>x</sub> sites and UO<sub>2</sub><sup>x+</sup>, as well as the presence of sodium ions allows the formation of Na<sub>2</sub>O(UO<sub>3</sub>·H<sub>2</sub>O)<sub>x</sub> precipitate during electrocatalysis.

The results above validate the practical adsorption–electrocatalysis technology introduced here for uranium extraction from seawater, which was based on amidoxime groups, isolated FeN<sub>x</sub> sites embedded in hollow nitrogen-doped porous carbons, and electrochemical catalysis processes. Benefitting from these features, Fe–N<sub>x</sub>–C–R demonstrated excellent performance as an adsorbent–electrocatalyst for the extraction of uranium from seawater. To our knowledge, the developed system is the first to yield a U(VI) solid product (i.e., Na<sub>2</sub>O(UO<sub>3</sub>·H<sub>2</sub>O)<sub>x</sub>) during

uranium extraction from seawater via an adsorption–electrocatalysis redox process. Our system offers the advantage that the  $\text{Na}_2\text{O}(\text{UO}_3 \cdot \text{H}_2\text{O})_x$  product can be easily removed for the Fe–N<sub>x</sub>–C–R/carbon felt electrode for collection. Nuclear reactors use enriched  $\text{UO}_2$  in the form of pellets as fuel.  $\text{Na}_2\text{O}(\text{UO}_3 \cdot \text{H}_2\text{O})_x$  can be easily converted to  $\text{UO}_2$  by chemical/thermal processing. These results will encourage further development of other adsorption–electrocatalysis systems containing metal single-atom active sites and functional groups for the extraction of uranium and other scarce metals from oceans.

### 3. Conclusion

In summary, we have developed an adsorption–electrocatalysis technology for the efficient extraction of uranium from seawater. The adsorbent–electrocatalyst (Fe–N<sub>x</sub>–C–R) consists of hollow N-doped carbon capsules surface functionalized with single-iron sites (FeN<sub>x</sub>) and amidoxime groups. This surface functionalization imparted Fe–N<sub>x</sub>–C–R with hydrophilicity and a high binding affinity for uranyl ions, whilst the iron sites provided a reversible electron transfer platform for the eventual production of  $\text{Na}_2\text{O}(\text{UO}_3 \cdot \text{H}_2\text{O})_x$ , a U(VI) precipitate, in the process of electrocatalytic extraction of uranium from seawater. Detailed uranium recovery tests showed Fe–N<sub>x</sub>–C–R was a very promising catalyst for uranium mining from seawater. Our novel adsorption–electrocatalysis strategy for uranium extraction overcomes the limitations of traditional physicochemical adsorbents for the collection of uranium, which require costly elution steps to recover uranium and regenerate the adsorbent. Moreover, the results presented here would prompt the broader pursuit of other metal–nitrogen–carbon materials and their composites as adsorption–electrocatalysts in uranium extraction and other applications. Our current work identifies opportunities for the economical and efficient extraction of uranium from oceans.

### Supporting Information

Supporting Information is available from the Wiley Online Library or from the author.

### Acknowledgements

The authors gratefully acknowledge funding support from National Key Research and Development Program of China (2017YFA0207002 and 2016YFA0203200), North China Electric Power University (X99986), National Science Foundation of China (Grants 22006036), and the Beijing Outstanding Young Scientist Program (H.Y. and X.W.). Partial support from the Robert A. Welch Foundation (B–0027) is also acknowledged (S.M.). The authors thank the support from the 14W station in Shanghai Synchrotron Radiation Facility (SSRF), and the XAS beamline of the Australian Synchrotron.

Note: Figure 5 and 6 were reset on December 21, 2021. The subscript in the x-axis label of Figure 5b was corrected as  $c_0$  and the x-axis label of Figure 6c was corrected to refer to the reciprocal of Å. In addition, a typo in the name of the Freundlich model was also corrected. Similar mistakes were also reset in the Supporting Information in Figure S13 and Figure S16.

### Conflict of Interest

The authors declare no conflict of interest.

### Data Availability Statement

The data that support the findings of this study are available from the corresponding author upon reasonable request.

### Keywords

amidoxime, iron–nitrogen–carbon, metal–organic frameworks, seawater, uranium

Received: August 23, 2021  
Revised: September 25, 2021  
Published online: October 15, 2021

- [1] S. Chu, A. Majumdar, *Nature* **2012**, *488*, 294.
- [2] a) A. Adamantziades, I. Kessides, *Energy Policy* **2009**, *37*, 5149; b) K. Mayer, M. Wallenius, K. Lutzenkirchen, J. Horta, A. Nicholl, G. Rasmussen, P. van Belle, Z. Varga, R. Buda, N. Erdmann, J. V. Kratz, N. Trautmann, L. K. Fifield, S. G. Tims, M. B. Frohlich, P. Steier, *Angew. Chem., Int. Ed.* **2015**, *54*, 13452.
- [3] D. S. Sholl, R. P. Lively, *Nature* **2016**, *532*, 435.
- [4] a) H. Lindner, E. Schneider, *Energy Econ.* **2015**, *49*, 9; b) J. Kim, C. Tsouris, R. T. Mayes, Y. Oyola, T. Saito, C. J. Janke, S. Dai, E. Schneider, D. Sachde, *Sep. Sci. Technol.* **2013**, *48*, 367.
- [5] C. W. Abney, R. T. Mayes, T. Saito, S. Dai, *Chem. Rev.* **2017**, *117*, 13935.
- [6] a) M. J. Manos, M. G. Kanatzidis, *J. Am. Chem. Soc.* **2012**, *134*, 16441; b) S. Ma, L. Huang, L. Ma, Y. Shim, S. M. Islam, P. Wang, L. D. Zhao, S. Wang, G. Sun, X. Yang, M. G. Kanatzidis, *J. Am. Chem. Soc.* **2015**, *137*, 3670; c) M. L. Feng, D. Sarma, X. H. Qi, K. Z. Du, X. Y. Huang, M. G. Kanatzidis, *J. Am. Chem. Soc.* **2016**, *138*, 12578; d) M. J. Comarmond, T. E. Payne, J. J. Harrison, S. Thiruvoth, H. K. Wong, R. D. Aughterson, G. R. Lumpkin, K. Muller, H. Foerstendorf, *Environ. Sci. Technol.* **2011**, *45*, 5536; e) S. Zhao, Y. Yuan, Q. Yu, B. Niu, J. Liao, Z. Guo, N. Wang, *Angew. Chem., Int. Ed.* **2019**, *58*, 14979.
- [7] a) Y. Yue, R. T. Mayes, J. Kim, P. F. Fulvio, X. G. Sun, C. Tsouris, J. Chen, S. Brown, S. Dai, *Angew. Chem., Int. Ed.* **2013**, *52*, 13458; b) S. Das, S. Brown, R. T. Mayes, C. J. Janke, C. Tsouris, L. J. Kuo, G. Gill, S. Dai, *Chem. Eng. J.* **2016**, *298*, 125; c) H.-B. Pan, L.-J. Kuo, J. Wood, J. Strivens, G. A. Gill, C. J. Janke, C. M. Wai, *RSC Adv.* **2015**, *5*, 100715; d) S. D. Alexandratos, X. Zhu, M. Florent, R. Sellin, *Ind. Eng. Chem. Res.* **2016**, *55*, 4208; e) Q. Sun, B. Aguila, J. Perman, A. S. Ivanov, V. S. Bryantsev, L. D. Earl, C. W. Abney, L. Wojtas, S. Ma, *Nat. Commun.* **2018**, *9*, 1644; f) Q. Sun, Y. Song, B. Aguila, A. S. Ivanov, V. S. Bryantsev, S. Ma, *Adv. Sci.* **2021**, *8*, 2001573; g) Y. Song, C. Zhu, Q. Sun, B. Aguila, C. Abney, L. Wojtas, S. Ma, *ACS Cent. Sci.* **2021**, *7*, <https://doi.org/10.1021/acscentsci.1c00906>.
- [8] a) Y. Yuan, Y. Yang, X. Ma, Q. Meng, L. Wang, S. Zhao, G. Zhu, *Adv. Mater.* **2018**, *30*, 1706507; b) Z. Wang, Q. Meng, R. Ma, Z. Wang, Y. Yang, H. Sha, X. Ma, X. Ruan, X. Zou, Y. Yuan, G. Zhu, *Chem* **2020**, *6*, 1683; c) Z. Li, Q. Meng, Y. Yang, X. Zou, Y. Yuan, G. Zhu, *Chem. Sci.* **2020**, *11*, 4747; d) Z. Wang, R. Ma, Q. Meng, Y. Yang, X. Ma, X. Ruan, G. Z. Y. Yuan, *J. Am. Chem. Soc.* **2021**, *143*, 14523.
- [9] a) J. Zhang, H. Zhang, Q. Liu, D. Song, R. Li, P. Liu, J. Wang, *Chem. Eng. J.* **2019**, *368*, 951; b) L. Chen, Z. Bai, L. Zhu, L. Zhang, Y. Cai, Y. Li, W. Liu, Y. Wang, L. Chen, J. Diwu, J. Wang, Z. Chai, S. Wang,



- ACS. *Appl. Mater. Interfaces* **2017**, *9*, 32446; c) W. Liu, X. Dai, Z. Bai, Y. Wang, Z. Yang, L. Zhang, L. Xu, L. Chen, Y. Li, D. Gui, J. Diwu, J. Wang, R. Zhou, Z. Chai, S. Wang, *Environ. Sci. Technol.* **2017**, *51*, 3911; d) Z.-Q. Bai, L.-Y. Yuan, L. Zhu, Z.-R. Liu, S.-Q. Chu, L.-R. Zheng, J. Zhang, Z.-F. Chai, W.-Q. Shi, *J. Mater. Chem. A* **2015**, *3*, 525.
- [10] a) S. O. Odoh, G. D. Bondarevsky, J. Karpus, Q. Cui, C. He, R. Spezia, L. Gagliardi, *J. Am. Chem. Soc.* **2014**, *136*, 17484; b) L. Zhou, M. Bosscher, C. Zhang, S. Ozcubukcu, L. Zhang, W. Zhang, C. J. Li, J. Liu, M. P. Jensen, L. Lai, C. He, *Nat. Chem.* **2014**, *6*, 236; c) Y. Yuan, T. Liu, J. Xiao, Q. Yu, L. Feng, B. Niu, S. Feng, J. Zhang, N. Wang, *Nat. Commun.* **2020**, *11*, 5708.
- [11] a) W. R. Cui, C. R. Zhang, W. Jiang, F. F. Li, R. P. Liang, J. Liu, J. D. Qiu, *Nat. Commun.* **2020**, *11*, 436; b) W. R. Cui, F. F. Li, R. H. Xu, C. R. Zhang, X. R. Chen, R. H. Yan, R. P. Liang, J. D. Qiu, *Angew. Chem., Int. Ed.* **2020**, *59*, 17684; c) W.-R. Cui, C.-R. Zhang, R.-H. Xu, X.-R. Chen, R.-H. Yan, W. Jiang, R.-P. Liang, J.-D. Qiu, *ACS EST Water* **2021**, *1*, 440; d) Y. Li, X. Guo, X. Li, M. Zhang, Z. Jia, Y. Deng, Y. Tian, S. Li, L. Ma, *Angew. Chem., Int. Ed.* **2020**, *59*, 4168; e) Q. Sun, B. Aguila, L. D. Earl, C. W. Abney, L. Wojtas, P. K. Thallapally, S. Ma, *Adv. Mater.* **2018**, *30*, 1705479.
- [12] a) D. Shao, G. Hou, J. Li, T. Wen, X. Ren, X. Wang, *Chem. Eng. J.* **2014**, *255*, 604; b) A. F. Ismail, M.-S. Yim, *Nucl. Eng. Technol.* **2015**, *47*, 579; c) F. Wang, H. Li, Q. Liu, Z. Li, R. Li, H. Zhang, L. Liu, G. A. Emelchenko, J. Wang, *Sci. Rep.* **2016**, *6*, 19367; d) Y. Yue, X. Sun, R. T. Mayes, J. Kim, P. F. Fulvio, Z. Qiao, S. Brown, C. Tsouris, Y. Oyola, S. Dai, *Sci. China: Chem.* **2013**, *56*, 1510.
- [13] S. Yang, P. Zong, J. Hu, G. Sheng, Q. Wang, X. Wang, *Chem. Eng. J.* **2013**, *214*, 376.
- [14] Y. Yuan, Q. Yu, S. Yang, J. Wen, Z. Guo, X. Wang, N. Wang, *Adv. Sci.* **2019**, *6*, 1900961.
- [15] a) D. Wang, J. Song, S. Lin, J. Wen, C. Ma, Y. Yuan, M. Lei, X. Wang, N. Wang, H. Wu, *Adv. Funct. Mater.* **2019**, *29*, 1901009; b) R. Li, L. Pang, H. Ma, X. Liu, M. Zhang, Q. Gao, H. Wang, Z. Xing, M. Wang, G. Wu, *J. Radioanal. Nucl. Chem.* **2016**, *311*, 1771.
- [16] C. Liu, P.-C. Hsu, J. Xie, J. Zhao, T. Wu, H. Wang, W. Liu, J. Zhang, S. Chu, Y. Cui, *Nat. Energy* **2017**, *2*, 17007.
- [17] a) S. Yuan, J. L. Shui, L. Grabstanowicz, C. Chen, S. Commet, B. Repragle, T. Xu, L. Yu, D. J. Liu, *Angew. Chem., Int. Ed.* **2013**, *52*, 8349; b) J. Li, S. Ghoshal, W. Liang, M.-T. Sougrati, F. Jaouen, B. Halevi, S. McKinney, G. McCool, C. Ma, X. Yuan, Z.-F. Ma, S. Mukerjee, Q. Jia, *Energy Environ. Sci.* **2016**, *9*, 2418; c) Y. Chen, S. Ji, Y. Wang, J. Dong, W. Chen, Z. Li, R. Shen, L. Zheng, Z. Zhuang, D. Wang, Y. Li, *Angew. Chem., Int. Ed.* **2017**, *56*, 6937; d) H. Yang, X. Chen, W. T. Chen, Q. Wang, N. C. Cuello, A. Nafady, A. M. Al-Enizi, G. I. N. Waterhouse, G. A. Goenaga, T. A. Zawodzinski, P. E. Kruger, J. E. Clements, J. Zhang, H. Tian, S. G. Telfer, S. Ma, *ACS Nano* **2019**, *13*, 8087; e) W. Wang, Q. Jia, S. Mukerjee, S. Chen, *ACS Catal.* **2019**, *9*, 10126; f) X. Wan, X. Liu, Y. Li, R. Yu, L. Zheng, W. Yan, H. Wang, M. Xu, J. Shui, *Nat. Catal.* **2019**, *2*, 259.
- [18] a) S. R. Venna, J. B. Jasinski, M. A. Carreon, *J. Am. Chem. Soc.* **2010**, *132*, 18030; b) H. Yang, S. J. Bradley, A. Chan, G. I. Waterhouse, T. Nann, P. E. Kruger, S. G. Telfer, *J. Am. Chem. Soc.* **2016**, *138*, 11872; c) H. Yang, S. J. Bradley, X. Wu, A. Chan, G. I. N. Waterhouse, T. Nann, J. Zhang, P. E. Kruger, S. Ma, S. G. Telfer, *ACS Nano* **2018**, *12*, 4594.
- [19] a) X. Lu, S. He, D. Zhang, A. T. Reda, C. Liu, J. Feng, Z. Yang, *RSC Adv.* **2016**, *6*, 101087; b) X. Yang, J. Li, J. Liu, Y. Tian, B. Li, K. Cao, S. Liu, M. Hou, S. Li, L. Ma, *J. Mater. Chem. A* **2014**, *2*, 1550.
- [20] X. Jin, C. Yu, Y. Li, Y. Qi, L. Yang, G. Zhao, H. Hu, *J. Hazard. Mater.* **2011**, *186*, 1672.
- [21] a) A. Zitolo, V. Goellner, V. Armel, M. T. Sougrati, T. Mineva, L. Stievano, E. Fonda, F. Jaouen, *Nat. Mater.* **2015**, *14*, 937; b) U. I. Kramm, M. Lefevre, N. Larouche, D. Schmeisser, J. P. Dodelet, *J. Am. Chem. Soc.* **2014**, *136*, 978.
- [22] G. Paolucci, G. Marangoni, G. Bandoli, D. A. Clemente, *J. Chem. Soc., Dalton Trans.* **1980**, 459.
- [23] N. T. Tavengwa, E. Cukrowska, L. Chimuka, *Toxicol. Environ. Chem.* **2016**, *98*, 1.
- [24] a) K. Yuan, E. S. Ilton, M. R. Antonio, Z. Li, P. J. Cook, U. Becker, *Environ. Sci. Technol.* **2015**, *49*, 6206; b) P. Herasymenko, *Trans. Faraday Soc.* **1928**, *24*, 272.
- [25] D. W. Wester, J. C. Sullivan, *Inorg. Chem.* **1980**, *19*, 2838.